European Hyperloop Week 2026: Aerodynamics Technical Report

Jonathan Distler[1] Kiran Foster[1]

May 2025

[1] Cornell University, Duffield College of Engineering

Contents

1 Introduction **1**

2 Mini-Pod Fabrication **2**
2.1 Lessons from Mini-Pod Fabrication 2

3 Aeroshell as a Pressure-Vessel **3**

4 Full-Pod Aeroshell **10**
4.1 Derivation 10
4.1.1 X-Momentum Balance 10
4.1.2 Reynolds Number 11
4.2 Flow Regions 11
4.2.1 Free-Stream Region 11
4.2.2 Stagnation Region 12
4.2.3 Boundary Layer Region 13
4.2.4 Y-Component Around Body 13
4.2.5 Adverse Pressure Gradient Region 13
4.2.6 Boundary Layer Separation 14
4.2.7 Wake Behind the Body 15
4.3 Simulation 15
4.3.1 Simulation Setup 15
4.3.2 Simulation Results 16
4.3.3 Simulation Analysis 17
4.4 Material Selection 18
4.5 Fabrication Process 18

Abstract

Cornell Hyperloop's Aerodynamic Team presents the design, analysis, and fabrication of an aeroshell system optimized for operation in imperfect vacuum conditions. Key considerations include vacuum pressure loading, outgassing behavior, and aerodynamic performance. Analytical methods—comprising rigid pressure vessel calculations and solutions to the Navier–Stokes X-momentum equation—are employed alongside computational fluid dynamics (CFD) and finite element analysis (FEA) to validate performance predictions. The study details the development of a scale model and the translation of these methods to a full-scale aeroshell, highlighting design trade-offs and fabrication strategies. Results emphasize optimizations in cost, aerodynamic efficiency, and structural weight, demonstrating a balanced approach to high-performance aeroshell design.

1 Introduction

Our process started by designing methods for a mini-pod aeroshell. This involved scaling down many of our fabrication methods to the tune of a 23.6% length-wise and 31.2% width-wise. The goal of this project was to better understand failure-modes in our fabrication methods, as well as provide a low-cost low-risk alternative to expending valuable time and money on unproven techniques on a larger system.

Our previous year's aeroshell fabrication process involved taking a large foam block (12 feet by 6 feet) and cutting it into discrete sections each matching the contour of the aeroshell CAD model at each appropriate section. This provided many failures modes. Firstly, it was difficult to match the foam sections up properly with one another given their size and weight. Secondly, it was hard to create a vacuum for the carbon-fiber layup, so our carbon-fiber shell was not very smooth as was expected. Finally, it was difficult to take off the shell from the convex body given its size and our adhesion methods to the foam. So, going forward, we were going to do the body in one piece to avoid mismatches in our blocking, we were going to make it easier to sustain a vacuum (through multiple vacuum entry ports and smarter geometries for vacuums), and we were going to make the hull convex rather than concave to improve our resolvability.

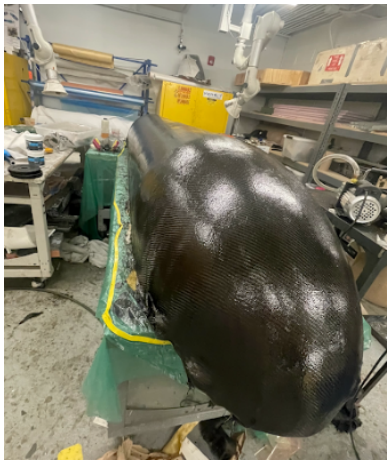


Figure 1: Convex Hyperloop Aeroshell Layup

2 Mini-Pod Fabrication

Firstly, we wanted to address the concavity of our aeroshell system. Opting for a concave system (often referred to as a female mold), we researched similar systems that had been built, and many of them used a skeleton system with reinforcements running length-wise along the aeroshell. Our design principle followed these practices with a very simple geometry to improve manufacturability. Additionally, we are going to try to implement a strip-planking methodology, which involves very think strips of plywood laid length-wise along the skeleton. When cut thin enough, the discrete sections can approximate a curved profile (much in the same ways a Reimann sum can approximate more sophisticated profiles with a very thin δx).

2.1 Lessons from Mini-Pod Fabrication

The main lessons taken from fabricating a mini-pod come down to the idea that the nose is the most difficult part to manufacture in terms of the allotted resources for the nose versus other parts of the aeroshell, difficulty in creating the nose contour shape, and the difficulty of getting the prescribed contours after sanding the nose for smoothness (in order to improve dynamic viscous losses). Taking these lessons, we opted for a single-nosed aeroshell with a very basic geometry along the axial direction, with a sheared face along the trailing edge. The trailing edge was used to reduce the fabrication constraints that come with building a nose, and it was thought that the

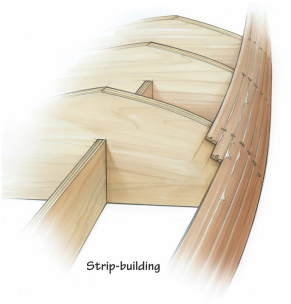


Figure 2: Strip Planking to Approximate Curvature with Discrete Planks

Source: WoodenBoat School [3]

trailing edge would have little influence on the performance of the aeroshell, although the following sections outline the incorrectness of that particular assumption. Finally, we learned much of the process associated with fabricating an aeroshell, including the materials and the cost for a mini-pod (which can be roughly scaled with surface-area for the full-pod version). The basics of our mold and skeleton design are outlined below:

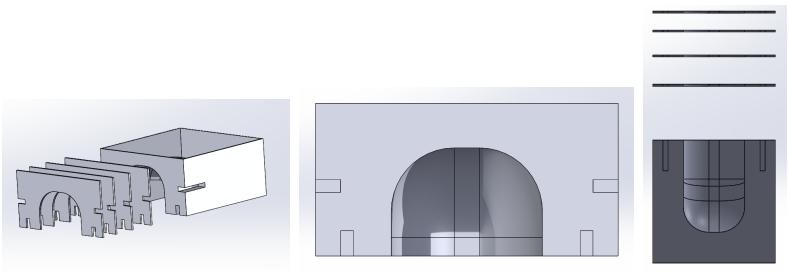


Figure 3: Mini-Pod Aeroshell Skeleton and Nose: Ortho, Front, and Top Views

3 Aeroshell as a Pressure-Vessel

Having spoken with ETH Zürich's Hyperloop Project Team (Swissloop), it seemed to be commonplace to approximate the aeroshell as a pressure vessel with the length not an order of magnitude longer than the width, such that the projected minor-axis of the aeroshell's elliptical shape isn't significantly smaller than the major-axis of the ellipse projected onto the

xy plane. With the aeroshell considered as a pressure vessel, the vacuum provides a force against the exterior of the aeroshell. Using that in mind, we decided to model the main hull of the shell as a pressure-vessel. Using the dimensions of our most up-to-date CAD model of our entire pod, we finalized on initial dimensions of an aeroshell hull of 1.8669 m long with an outer-radius of .254 m and a thickness of .01 m (10 mm). Using the idealized pressure-vessel equations for hoop and longitudinal stress we determined the following relationships:

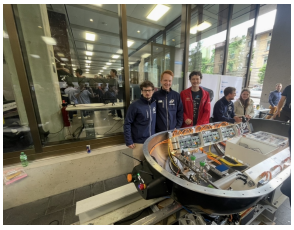


Figure 4: Swissloop Aeroshell (length greater than width, but not by an order of magnitude)

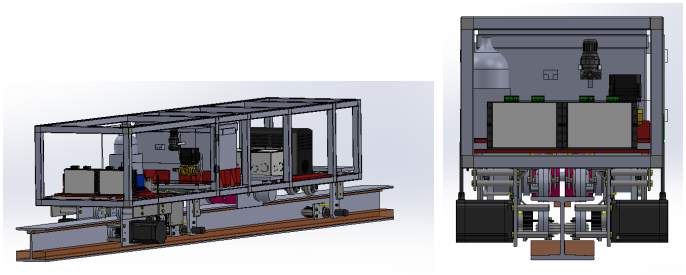


Figure 5: Full Pod Assembly without Aeroshell: Ortho and Front Views

Hoop and Longitudinal Stress Calculations

$$
\begin{aligned}
P_{\text{ext}} &= 0 \\
P_{\text{int}} &= 101325\,\text{Pa}\ (1\,\text{atm}) \\
t &= 0.01\,\text{m} \\
\sigma_h &= \frac{Pr}{t} = 2.6\,\text{MPa} \\
\sigma_l &= \frac{Pr}{2t} = 1.3\,\text{MPa}
\end{aligned}
$$

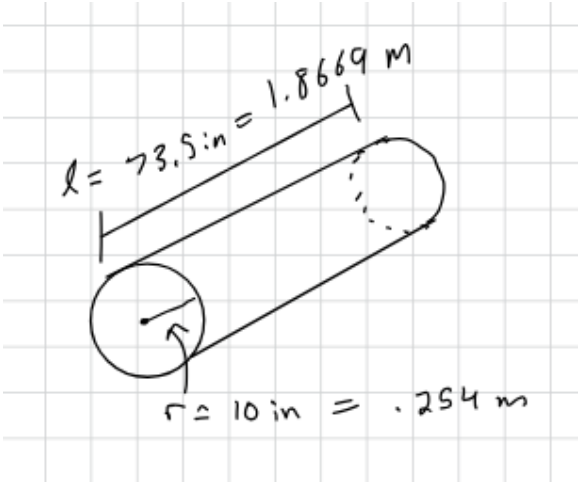


Figure 6: Pressure Vessel Mock-Up

Thus, with the hoop stress being the limiting constraint in factor-of-safety calculations, we moved forward with our calculations. In the limit as the pressure differential goes towards zero, the shell would need the strength to only combat external forces and support the weight of itself. Due to the external vacuum, the pod will experience a maximum hoop stress of 2.6 MPa; with equal internal and external pressures, the shell would only experience structural forces unrelated to bursting.

As for other considerations, in the event that the internal pressure were greater than the external pressure, the pressurized vessel would be subject to a stiffening effect, which signifies a tendency to sag underneath its own weight. In the event the external pressure equals the internal pressure, the vessel is subject to greater sagging along its length due to supporting its own weight. The following calculations outline considerations for carbon-fiber (our previously used material) as our idealized material for construction:

Weight per Unit Length
Outer radius: $r_o = 0.528$ m
Inner radius: $r_i = 0.508$ m
Length: $L = 1.867$ m

$$W = \rho g \frac{\pi}{4} \left(r_o^2 - r_i^2\right)$$
$$W = \rho g \frac{\pi}{4} \left(0.528^2 - 0.508^2\right)$$
$$W = 279 \text{ N/m}$$

Max Bending Moment

$$M = \frac{WL^2}{8}$$
$$M = 121 \text{ N} \cdot \text{m}$$

Section Modulus

$$Z = \frac{\pi \left(0.528^4 - 0.508^4\right)}{32 \cdot 0.528}$$
$$Z = 0.0021 \text{ m}^3$$

Sagging Stress

$$\sigma_b = 0.06 \text{ MPa}$$

at a wall thickness of 10 mm (0.01 m)

Having a baseline of the hand-calculations to compare with analytical solutions derived from ANSYS. All of the aforementioned results are well above the conditions we would be putting our system, thus there would be a very high factor-of-safety in regards to all failure-modes. This is typically the best practice to understand the modes of failure for the system and compare that with the finite element methods of ANSYS. We were most interested in the deformations, normal stresses, and the principle stresses of the system considering carbon fiber's anisotropic deformation to failure and its anisotropic stress to failure. As for the setup, we used a pinned-pinned geometry with an internal pressure of 101325 Pa, and using carbon-fiber with a Young's Modulus of 230 GPa. Additionally, we tested other materials in simulation to provide a direct comparison with the carbon-fiber setup, which could provide cheaper alternatives, but as is seen, they do not have the necessary deformations to failure and deform too much under our particular loading conditions. As is seen in all of the finite-element analysis results, the carbon fiber has very little deformation and very low internal stress in its maximum principle direction, even underneath its own weight. Also,

comparatively to a much cheaper alternative in PLA, it greatly outperforms in regards to total deformation and maximum principle stress.

Assuming a composite material, using a Carbon Fiber with a Young's Modulus of 230 GPa, an ultimate stress of 1800 Mpa, and a max stress in the system's setup of 3.8879 MPa.

Factor of Safety Calculations

$$FoS = \frac{\sigma ult}{\sigma max}$$

$$Fos = \frac{1800MPa}{3.8879MPa}$$

$$Fos = 463 >> 1$$

Total Deformation

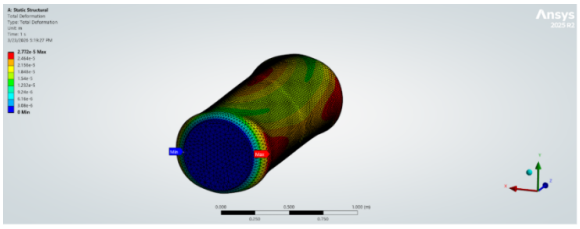


Figure 7: Total Deformation (Ortho. View)

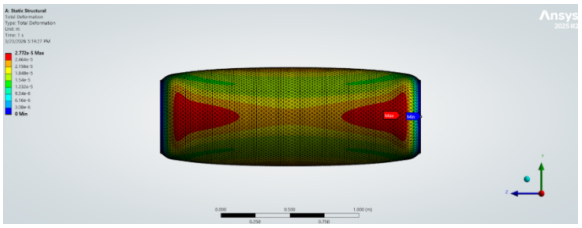


Figure 8: Total Deformation (Side View)

Maximum Principle Stress
Normal Stress Along X-Direction
Total Deformation Comparison (Carbon Fiber vs. PLA)
Maximum Principle Stress Comparison (Carbon Fiber vs. PLA)

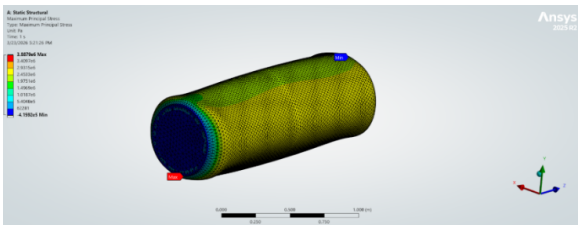


Figure 9: Maximum Principle Stress

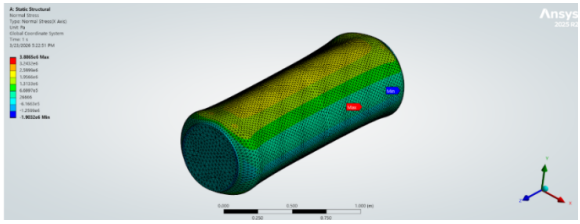


Figure 10: Normal Stress Along X-Direction (Ortho. View)

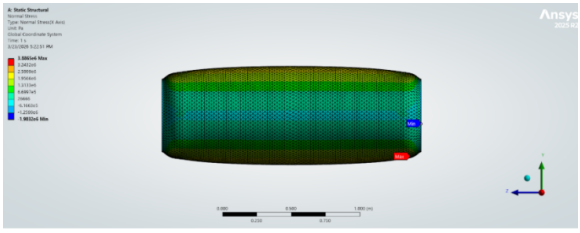


Figure 11: Normal Stress Along X-Direction (Side View)

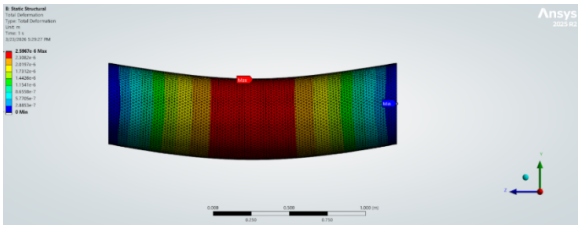


Figure 12: Carbon Fiber Deformation

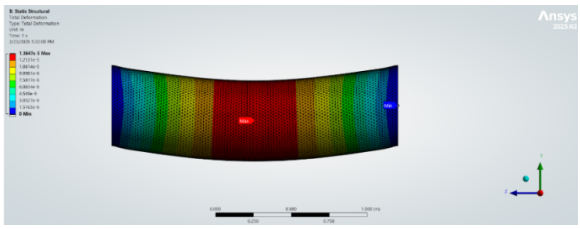


Figure 13: PLA Deformation

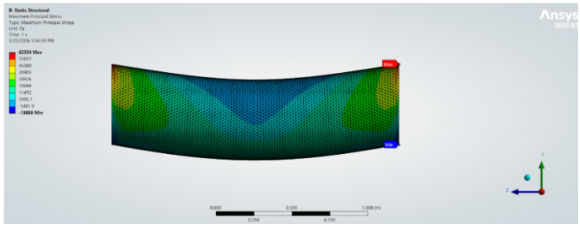


Figure 14: Carbon Fiber Maximum Principle Stress

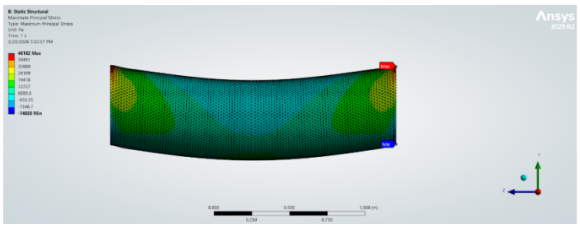


Figure 15: PLA Maximum Principle Stress

4 Full-Pod Aeroshell

4.1 Derivation

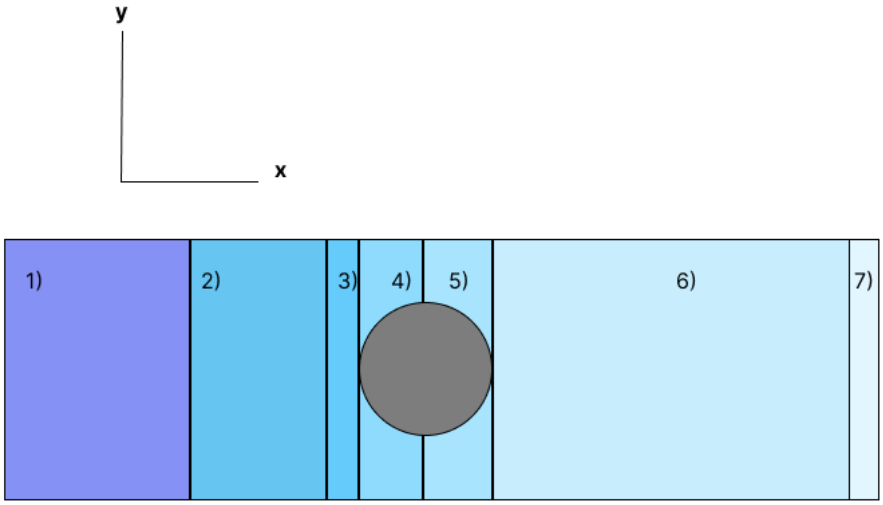


Figure 16: Generalized Regions of Flow for a Bluff-Body; Representing the Front of Aeroshell

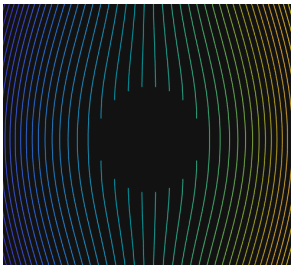


Figure 17: Potential Flow Around a Cylinder

4.1.1 X-Momentum Balance

The general X-momentum equation for incompressible flow is:

$$\frac{\partial u}{\partial t} + \left(u\frac{\partial u}{\partial x} + v\frac{\partial u}{\partial y} \right) = -\frac{\partial p}{\partial x} + \left(\frac{\partial^2 u}{\partial x^2} + \frac{\partial^2 u}{\partial y^2} \right) \tag{1}$$

where u and v are the velocity components in the x and y directions, respectively, and p is the pressure.

4.1.2 Reynolds Number

Assuming a moderate vacuum for the Hyperloop, the following properties are used:

- Density: $\rho = 0.01$ kg/m^3
- Characteristic length: $L = 2$ m
- Velocity: $V = 90$ m/s
- Dynamic viscosity: $\mu = 1.8 \times 10^{-5}$ Pa $\cdot$ s

The Reynolds number is calculated as:

$$\text{Re} = \frac{\rho V L}{\mu} = \frac{0.01 \cdot 90 \cdot 2}{1.8 \times 10^{-5}} \approx 100{,}000 \tag{2}$$

Since the Reynolds number is large, the flow is in the high Reynolds number regime (also referred to as the potential flow regime), and bluff body approximations can be applied.

4.2 Flow Regions

4.2.1 Free-Stream Region

Assuming 2D, steady-state flow with $U = [u, 0]$, the X-momentum equation reduces to:

$$0 = -\frac{\partial p}{\partial x} \tag{3}$$

indicating constant pressure upstream of the body.

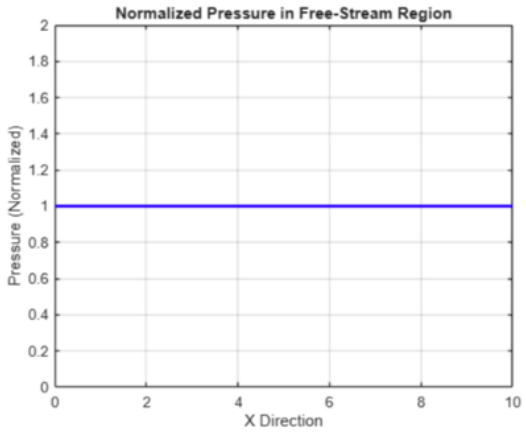


Figure 18: Normalized Pressure in Free-Stream Region

4.2.2 Stagnation Region

Near the nose of the aeroshell, a velocity gradient appears with $\partial u/\partial x < 0$. Assuming negligible viscous effects:

$$u\frac{\partial u}{\partial x} = -\frac{\partial p}{\partial x} \tag{4}$$

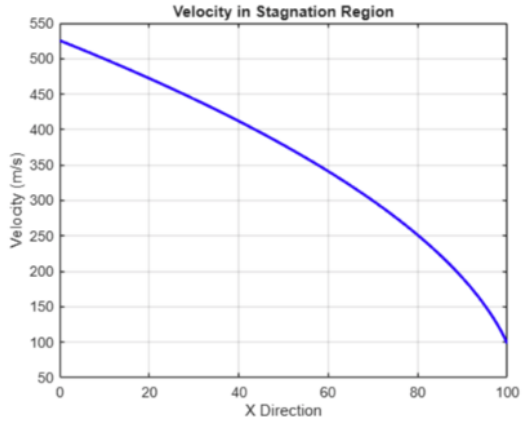


Figure 19: Velocity in the X-Direction within the Stagnation Region; Using implicit variables from derivation setup

4.2.3 Boundary Layer Region

Within the boundary layer, due to the no-slip condition at the wall, the x-velocity is zero at the surface and:

$$u\frac{\partial u}{\partial x} + v\frac{\partial u}{\partial y} = -\frac{\partial p}{\partial x} + \frac{\partial^2 u}{\partial y^2} \tag{5}$$

4.2.4 Y-Component Around Body

As the fluid moves around the body edges, a y-velocity develops, and the X-momentum simplifies to:

$$u\frac{\partial u}{\partial x} + v\frac{\partial u}{\partial y} = -\frac{\partial p}{\partial x} \tag{6}$$

indicating pressure decreases and fluid accelerates.

4.2.5 Adverse Pressure Gradient Region

Past the widest part of the body, the pressure increases, decelerating the fluid. Within the boundary layer:

$$u\frac{\partial u}{\partial x} + v\frac{\partial u}{\partial y} = -\frac{\partial p}{\partial x} + \frac{\partial^2 u}{\partial y^2} \tag{7}$$

Assuming a pressure gradient of zero, the term becomes:

$$u\frac{\partial u}{\partial x} + v\frac{\partial u}{\partial y} = \frac{\partial^2 u}{\partial y^2} \tag{8}$$

Using a similarity with the Blasius solution leads to an analytical form using the stream function:

$$u = \frac{\partial \Psi}{\partial y}, \qquad v = -\frac{\partial \Psi}{\partial x} \tag{9}$$

Substituting into the governing equation gives:

$$\frac{\partial u}{\partial x} = \frac{\partial^2 \Psi}{\partial x \partial y}$$

$$\frac{\partial u}{\partial y} = \frac{\partial^2 \Psi}{\partial y^2}$$

$$\frac{\partial^2 u}{\partial y^2} = \frac{\partial^3 \Psi}{\partial y^3}$$

$$u\frac{\partial u}{\partial x} = \left(\frac{\partial \Psi}{\partial y}\right)\left(\frac{\partial^2 \Psi}{\partial x \partial y}\right)$$

$$v\frac{\partial u}{\partial y} = -\left(\frac{\partial \Psi}{\partial x}\right)\left(\frac{\partial^2 \Psi}{\partial y^2}\right)$$

Thus, the final equation is as follows:

$$\left(\frac{\partial \Psi}{\partial y}\right)\left(\frac{\partial^2 \Psi}{\partial x \partial y}\right) - \left(\frac{\partial \Psi}{\partial x}\right)\left(\frac{\partial^2 \Psi}{\partial y^2}\right) = \frac{\partial^3 \Psi}{\partial y^3}$$

4.2.6 Boundary Layer Separation

After the body, wall shear stress drops to zero. The boundary layer can no longer overcome the adverse pressure gradient, resulting in separation:

$$0 = -\frac{\partial p}{\partial x} + \frac{\partial^2 u}{\partial y^2} \tag{10}$$

The laplacian, assuming no pressure gradient becomes:

$$u_y = c_1 y + c_2 \tag{11}$$

With the following boundary conditions:

$$u_y(\infty) = u_0$$

$$u_y(0) = u_0$$

Thus,

$$c_2 = u_0$$

$$u_y(x) = u(0)$$

4.2.7 Wake Behind the Body

Far downstream, the pressure gradient becomes negligible, flow is primarily in the x-direction, and temporal variations dominate:

$$\frac{\partial u}{\partial t} + \left(u\frac{\partial u}{\partial x} + v\frac{\partial u}{\partial y} \right) = -\frac{\partial p}{\partial x} \tag{12}$$

This equation has no closed-form solution and although it resembles a 1D-Burgers-type solution, its v-velocity does not satisfy that condition.

4.3 Simulation

With the analytical solutions for many of the regions of the flow stream, we had a good comparison tool for our CFD model, in order to compare the fidelity of the simulation. The main issue that arose is D'Alembert's paradox, in the potential flow regime, which predicts 0 drag force regardless of the external fluid's viscosity due to a limited number of constraining equations (and the need to specify the no-penetration constraint: $\hat{n}$ * $\mathbf{u}$=0), thus our analytical solutions could not predict drag for the case the vacuum wasn't completely perfect. So, we used the ANSYS Workbench tool, with a very hemispherical design for a higher-stability within the discretized finite-difference scheme underpinning most ANSYS software. We had chosen the embedded CFD software within ANSYS Workbench rather than the more traditional ANSYS Fluent because of the ease of exporting complicated geometries without having to project the model into 2D geometries.

4.3.1 Simulation Setup

To define the governing equations for the simulation, we had used the "air" as our fluid; we recognize that the Hyperloop would ideally be operating in a vacuum, but no vacuum is free of all matter, so we thought for the time being that a simulation involving limited matter within the system would suggest marginal benefits associated with more aerodynamic aeroshell designs. For the aeroshell's material, we used "Aluminum alloy, wrought" because of its similar roughness (both on $\mathcal{O}(10^{-6}m)$) [1], meaning they should ideally have similar dynamic viscosity and similar losses. Finally, we simulated an inlet velocity of roughly 480 m/s, which is similar to speeds experienced by many of the MagLev trains throughout world [2]. Finally, the inlet was placed at the front-nose of the aeroshell, and the bottom of the aeroshell was constrained to be a static boundary; we only simulated half of the shell because eventually we were going to add a symmetric second-shell such that

the full chassis was covered, simulating with less geometry typically improves results, so its commonplace to avoid unnecessary symmetry and mirror the results in post-processing.

4.3.2 Simulation Results

As for the results, we were trying to understand the stream function and its associated streamlines of our aeroshell, to determine the separation point of the flow (proportional to the form-drag of a body). We also wanted to understand the structure of the fluid going over our aeroshell for future design considerations, such as possibly incorporating dimples (e.g. golf-balls) to move back the separation point and improve the form-drag coefficient. The images of relevant properties determined from the simulation are shown below:

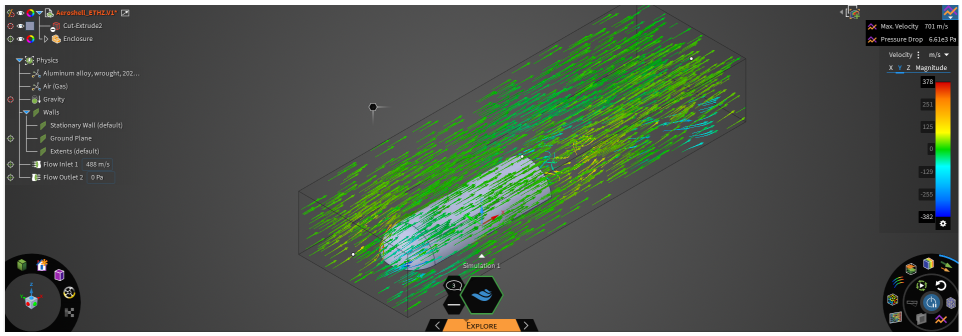


Figure 20: Streamlines on the Hemispherical Aeroshell

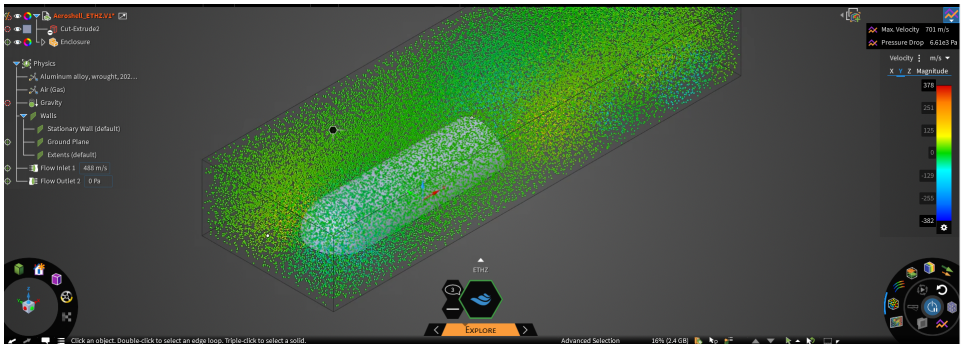


Figure 21: Velocity Contours on the Hemispherical Aeroshell

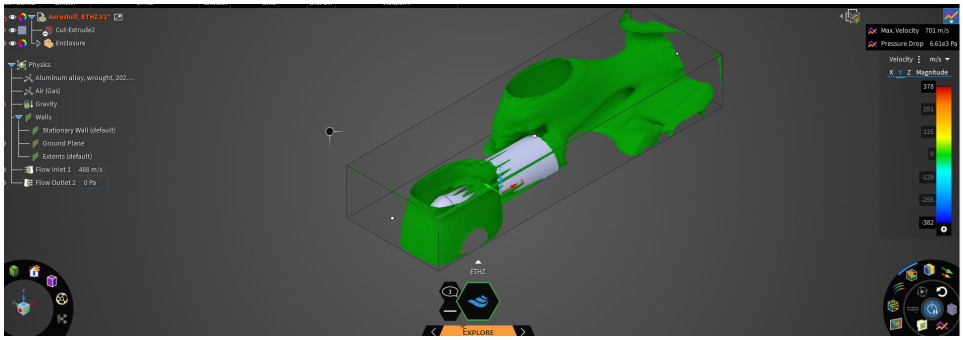


Figure 22: Pressure Contours on the Hemispherical Aeroshell

4.3.3 Simulation Analysis

As can be seen in the simulations, the velocity streamlines are all similar and on the same order of magnitude (roughly 380 m/s). Similarly, it can be seen that there is separation along the backside of the aeroshell, which makes sense intuitively given the nearly infinite gradient along the trailing edge. This could be remedied in the future with a gentler slope along the back-side or by using aforementioned techniques to push back the separation point. Similarly, the pressure contours show roughly constant pressure along the nose and along the top of the trailing edge which follows from Bernoulli's principle along a streamline (which is only applicable during incompressible and non-viscous flows), meaning that our aeroshell represents a very low-loss system. Furthermore, our simulation was validated by the previous analytical solutions, showing that along the front of the aeroshell the fluid is expected to be uniform and far away from the end of the aerosehll, the fluid again should be uniform. At the nose, the fluid should stagnate causing a high pressure (as evidenced in the pressure contour on the nose), and along the boundary layer the normalized pressure should be the same (again evidenced by a equipotential pressure along the top-side). Then, along the very back-side the pressure decreases, often causing an adverse pressure gradient and separation. In short, the simulation was validated by the analytical solutions previously derived in the x-momentum balance using the Navier-Stokes equation. From these solutions we understand that most of the inefficiencies in our aeroshell come from the sharp trailing edge which was chosen for ease of manufacturing. This produces a very delicate trade-off between the ease of manufacturing the aerosehll's body and the inefficiencies exacerbated by the imperfect aeroshell design. Going forward we decided that the ease of manufacturing won out in this particular in-

stance given cost scales non-linearly with complexity on the nose. We also recognized that the deviates more from an ideal pressure-vessel, however, supports can be added appropriately within the aeroshell body to improve structural integrity which is orders of magnitude cheaper than adding a more complicated geometry along the back of the aeroshell.

4.4 Material Selection

The following is the breakdown of necessary materials used in the mini-pod fabrication scaled by the ratio of surface area of the aeroshell to the mini-pod. This was derived empirically from scaling the amount we found useful on the mini-pod.

Part	Material	Qty	Est. Cost ($)	Function
Nose Piece	High-density foam	1	10–30	Lightweight core, shapes aerodynamic nose
Inner Planks	Balsa wood	8	40–80	Core structure, provides stiffness with low weight
Aligning Planks	Wood (TBD)	6	20–50	Maintains alignment during assembly
Top Frame	Wood (TBD)	1	15–40	Structural support and load distribution
Screws	Steel (TBD)	–	10–20	Mechanical fastening of components
Mastic	Sealant tape	–	15–30	Seals vacuum bag, prevents air leaks
Epoxy	Resin + hardener	2	50–120	Matrix material binding composite layers
Acetone	Solvent	1	10–20	Cleaning tools and surfaces
Duratec	Surface primer	1	40–80	Mold surface finish and release prep
Peel Ply	Nylon fabric	1	10–25	Creates textured surface for bonding
Breather	Polyester fabric	1	10–25	Allows air flow in vacuum bagging
Kevlar	Aramid fiber sheet	1	30–80	Impact resistance layer
Carbon Fiber	Composite fabric	1	40–120	High strength-to-weight structural layer
Plywood (thick)	0.709” sheet	5–6	300–380	Mold or base structure
Plywood (thin)	0.594” sheet	3	100–130	Secondary structural elements
Primer	Surface coating	2	40–90	Prepares mold for finishing
Wax	Mold release	1	25	Prevents part sticking to mold

Table 1: Bill of Materials with estimated costs and functions

Figure 23: Bill of Materials for the Aeroshell

4.5 Fabrication Process

The fabrication process is still ongoing, but at the moment, we have a skeleton laser-cut out of balsa wood, as well as thick plywood stripped down and laid over the balsa-wood skeleton to match the ideal contour of the aeroshell’s outer dimensions. The nose outline is being developed concurrently and we hope to have a working model developed out of foam within

the next 1-2 months. The CAD for the relevant setup is shown below, using a nearly identical methodology to the one designated for the mini-pod:

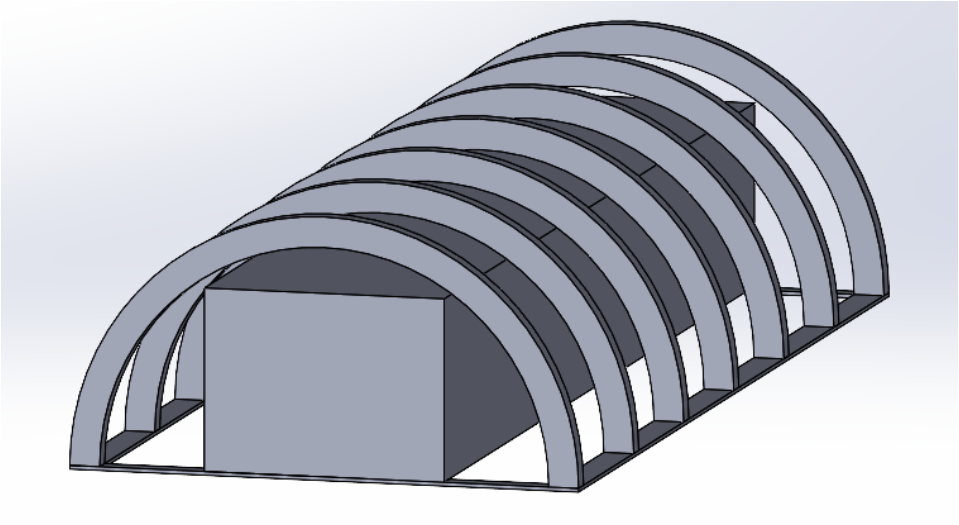


Figure 24: Balsa Wood Skeleton

references